CHEMISTRY OF MATERIALS

Article

pubs.acs.org/cm

Nitrogen and Iron-Codoped Carbon Hollow Nanotubules as High-Performance Catalysts toward Oxygen Reduction Reaction: A Combined Experimental and Theoretical Study

Bingzhang Lu,[†] Tyler J. Smart,[‡] Dongdong Qin,[§] Jia En Lu,[†] Nan Wang,[⊥] Limei Chen,[†] Yi Peng,[†] Yuan Ping,*[,†] and Shaowei Chen*[,†]

[†]Department of Chemistry and Biochemistry and [‡]Department of Physics, University of California, 1156 High Street, Santa Cruz, California 95064, United States

[§]Key Laboratory of Bioelectrochemistry & Environmental Analysis of Gansu Province, College of Chemistry and Chemical Engineering, Northwest Normal University, Lanzhou 730070, China

[⊥]New Energy Research Institute, School of Environment and Energy, South China University of Technology, Guangzhou Higher Education Mega Center, Guangzhou 510006, China

Supporting Information

ABSTRACT: Heteroatom-doped carbons represent a unique class of low-cost, effective catalysts for the electroreduction of oxygen, with a performance that may rival that of commercial Pt/C catalysts. In the present study, Fe and N codoped porous carbon nanotubules were prepared by controlled pyrolysis of tellurium nanowire-supported melamine formaldehyde polymer core−sheath nanofibers at elevated temperatures. Electron microscopic studies showed the formation of hollow carbon nanotubules with the outer diameter of 35−40 nm, inner diameter of 5−10 nm, and length of several hundred nanometers. Elemental mapping and spectroscopic measurements confirmed the doping of the carbon nanotubules with N and Fe including the formation of FeN_4 moieties. Electrochemical studies showed that the resulting Fe,N-codoped carbons exhibited much enhanced electrocatalytic activity toward oxygen reduction in alkaline media as compared to the counterparts doped with nitrogen alone and prepared in a similar fashion, and the one prepared at 800 °C stood out as the best among the series, with an activity even better than that of commercial Pt/C. Such a remarkable performance was ascribed to the FeN_4 moieties that facilitated the binding of oxygen species. This is further supported by results from DFT calculations, where relevant atomistic models were built based on experimental results and reaction free energies on various possible active sites were computed by first-principles calculations. The computational results suggested that for N-doped carbons, the active sites were the carbon atoms adjacent to nitrogen dopants, while for Fe,N-codoped carbon, the FeN_4 moieties were most likely responsible for the much enhanced electrocatalytic activity, in excellent agreement with experimental results. Significantly, from the electronic structure studies, it was found that the high density of states close to the Fermi level and high spin density played a critical role in determining the electrocatalytic activity.

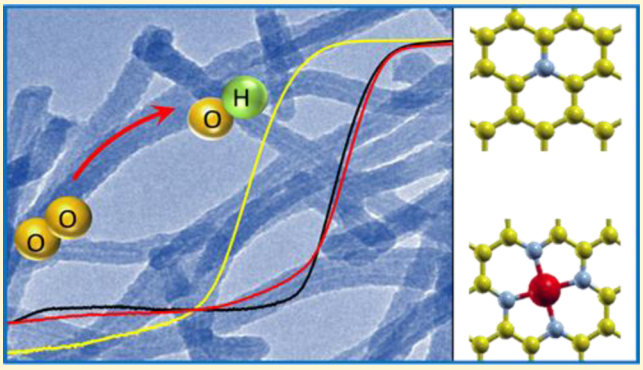

INTRODUCTION

Polymer electrolyte membrane fuel cells (PEMFCs) have attracted extensive interest as a viable energy technology for portable electronics as well as transportation because of the high efficiency in converting chemical energy in small organic fuel molecules to electricity.[1−6] During fuel cell operation, oxygen reduction reaction (ORR) at the cathode is a critical process that has been recognized as a major bottleneck limiting the fuel cell performance due to the complex reaction pathways and sluggish electron-transfer kinetics. To produce a current density sufficiently high for practical applications, Pt-based nanoparticles have been used extensively as the catalysts of choice for ORR. Nevertheless, wide applications of PEMFCs based on Pt catalysts have been hampered by the low natural abundance, high costs, and lack of long-term stability of platinum.[7−9] Lately, carbon-based materials have been found to exhibit apparent ORR activity and may serve as a promising candidate to replace Pt for ORR catalysis.[10−13] These carbon catalysts are generally doped with heteroatoms, such as N,[14] P,[15] B,[16] and S,[17] and the activity may be further enhanced by the incorporation of various transition metals such as Fe,[18] Co,[19] Ni,[20] and Cu.[21] Among these, Fe,N-codoped carbons

Received: March 28, 2017
Revised: June 6, 2017
Published: June 8, 2017

DOI: 10.1021/acs.chemmater.7b01265
Chem. Mater. 2017, 29, 5617−5628

stand out because of their remarkable ORR activity that may even rival that of commercial Pt/C catalysts.[22−31] Such carbon-based catalysts are generally prepared by controlled pyrolysis of selected precursors. Of these, template-assisted synthesis has been used rather extensively,[32] where the ORR activity has been found to be dependent on various structural parameters, such as the concentrations and molecular configurations of the dopants, and porosity, surface accessibility, and electrical conductivity of the carbon materials. For instance, Wei et al.[33] coated cellulose with an iron tannin framework ink and prepared Fe_3C/Fe−N−C nanocomposites by controlled pyrolysis at elevated temperatures with the addition of dicyandiamide. The materials exhibited a high onset potential of +0.98 V versus reversible hydrogen electrode (RHE) as well as high kinetic current density of 6.4 mA/cm^2 at +0.8 V. Ferrero et al.[18] exposed $FeCl_3$-impregnated silica particles to pyrrole vapors to produce Fe-polypyrrole nanoparticles, and pyrolysis of the resulting polymer hybrids led to the formation of Fe and N codoped porous carbons, which exhibited apparent ORR activity in both acid and base solutions. Yang et al.[34] pyrolyzed L-cysteine decorated C_3N_4 nanosheets and synthesized N-doped graphene nanoribbons as metal-free ORR catalysts, which exhibited a high onset potential +0.92 V and half-wave potential of +0.84 V versus RHE. Sa et al.[35] prepared Fe−N/C catalysts by pyrolysis of Fe(III)-porphyrin and carbon nanotube complexes with a SiO_2 coating, which displayed a high half-wave potential of +0.88 V along with good durability.

Despite the progress, the mechanistic origin, in particular, the role of the various N dopant configurations in ORR, has remained a matter of heated debate.[34,36] In addition, in Fe,N-codoped carbons, FeN_x, Fe_3C, or even carbon atoms have been proposed as the active centers for ORR.[37−40] In fact, a series of studies based on density functional theory (DFT) calculations has been carried out to resolve these issues,[41,42] yet it remains a challenge to correlate the structural models in DFT calculations to the experimental systems. This is the primary motivation of the present study where we combine experimental and theoretical approaches to unravel the catalytically active sites of Fe,N-codoped carbons for ORR in alkaline media.

In the present study, by controlled pyrolysis of core−sheath nanofibers with melamine-formaldehyde polymers supported on tellurium nanowire (Te NW) surfaces as the precursors, we successfully synthesized one-dimensional, porous, Fe,N-co-doped carbon nanotubules, which exhibited apparent ORR activity in alkaline media, with a performance comparable/superior to that of state-of-art Pt-free catalysts reported in recent literature.[18,33,40,43−45] The Te NWs were used as thermally removable nanowire templates,[46,47] largely because of the ease of preparation,[48,49] and low boiling point of tellurium (449 °C).[50] The formation of one-dimensional nanotubular structures is anticipated to facilitate both electron-transfer kinetics and mass-transfer of reaction intermediates, as compared to the random porous carbons in most prior research.[51] Computationally, relevant atomistic models were built where N-doped carbon was embedded with FeN_4 moieties based on experimental data from X-ray photoelectron spectroscopy (XPS) and electron microscopic measurements. First-principles calculations were carried out in the presence of implicit solvents to estimate the reaction free energies of each intermediate on various possible sites and overpotentials that showed excellent agreement with experimental data. The results suggested that the FeN_4 moieties were mostly likely the ORR active sites and played a major role in determining the observed ORR activity.

EXPERIMENTAL SECTION

Chemicals. Sodium tellurite (Na_2TeO_3, 99.5%, Alfa Aesar), melamine (99%, Acros Organics), hydrazine hydrate (N_2H_4, 64% v/v, Acros Organics), polyvinylpyrrolidone (PVP, K30, USB), sodium hydroxide (NaOH, Fisher Scientific), formaldehyde (37% v/v, Acros Organics), ammonia (35% in water, Acros Organics), and Pt/C (20 wt %, Alfa Aesar) were used as received. Water was supplied from a Barnstead Nanopure Water System (18.3 MΩ cm).

Synthesis of Te NWs. Te NWs were synthesized by adopting a literature procedure.[52] In a typical experiment, 0.0368 g of Na_2TeO_3 and 0.4 g of PVP were dissolved in 13 mL of nanopure water under vigorous stirring to form a homogeneous solution, into which were injected 1.35 mL of ammonia and 0.66 mL of N_2H_4. The solution was then transferred into a 20 mL Telfon-lined autoclave container and heated at 180 °C for 3 h. The autoclave was cooled down naturally before the product was collected by centrifugation at 3000 rpm for 2 min with the addition of a small amount of acetone and stored in a 4 °C refrigerator.

Synthesis of Te NW-Melamine Formaldehyde Polymer Core−Sheath Nanofibers. In brief, 12.5 mg of Te NWs prepared above was dispersed in 5 mL of water. Separately, 0.126 g of melamine together with 15 mL of water was added in a 50 mL round-bottom flask, and the solution was heated to 90 °C under magnetic stirring, into which were then injected the Te NWs solution, 20 μL of 0.2 M NaOH, and 0.53 mL of formaldehyde. The solution was heated at 90 °C for 7 h before being cooled down naturally. The product was collected by centrifugation at 5000 rpm for 5 min, washed with water and ethanol, and dried in a vacuum chamber for 24 h, which afforded Te NW-melamine formaldehyde polymer (Te-MF) core−sheath nanofibers.

Synthesis of Fe,N-Codoped Carbon Nanotubules. In a typical synthesis, 50 mg of the Te-MF nanofibers obtained above was dispersed in 1 mL of ethanol, along with 1 mg of $FeCl_3$. The mixture was sonicated for 1 h to form a homogeneous dispersion, which was then dried by a nitrogen flow and kept in a vacuum chamber for 12 h before being placed in a tube furnace and heated at a controlled temperature (600, 700, 800, or 900 °C) for 3 h at a heating rate of 5 °C/min. The nitrogen flow was maintained at 200 cc/min. The obtained samples were washed with water and ethanol three times and referred to as MF-Fe-T with T = 600, 700, 800, or 900. A control sample was also prepared in the same manner at the heating temperature of 900 °C but without the addition of $FeCl_3$, which was denoted as MF-900.

Characterization. Transmission electron microscopy (TEM) and elemental mapping studies were carried out with a FEI Tecnai TF20 microscope operated at 200 kV. XPS measurements were acquired by using a PHI X-tool instrument. Raman spectra were collected with a micro Raman Imaging Microscope with a laser wavelength of 632.8 nm.

Electrochemistry. Electrochemical measurements were carried out with a CHI 710 electrochemical workstation in a conventional three-electrode configuration. To prepare catalyst inks, in a typical experiment, 1 mg of the samples obtained above, together with 4 mg of carbon black and 10 μL of nafion, was dispersed in 1 mL of ethanol. The mixture was sonicated for at least 1 h to make a homogeneous dispersion. Then 10 μL of the ink was dropcast onto the glassy carbon disk of a rotating (gold) ring-(glassy carbon) disk electrode (RRDE, from Pine Instrument), corresponding to a catalyst loading of 40.65 μg/cm^2. When the catalyst film was dry, 4 μL of 20% nafion was added on top of the catalyst before the electrode was immersed into electrolyte solutions for data acquisition. A Ag/AgCl electrode in 0.1 M KCl was used as the reference electrode and a platinum coil as the counter electrode. The reference electrode was calibrated against a RHE, and all potentials in the present study were referred to this RHE.

DOI: 10.1021/acs.chemmater.7b01265
Chem. Mater. 2017, 29, 5617−5628

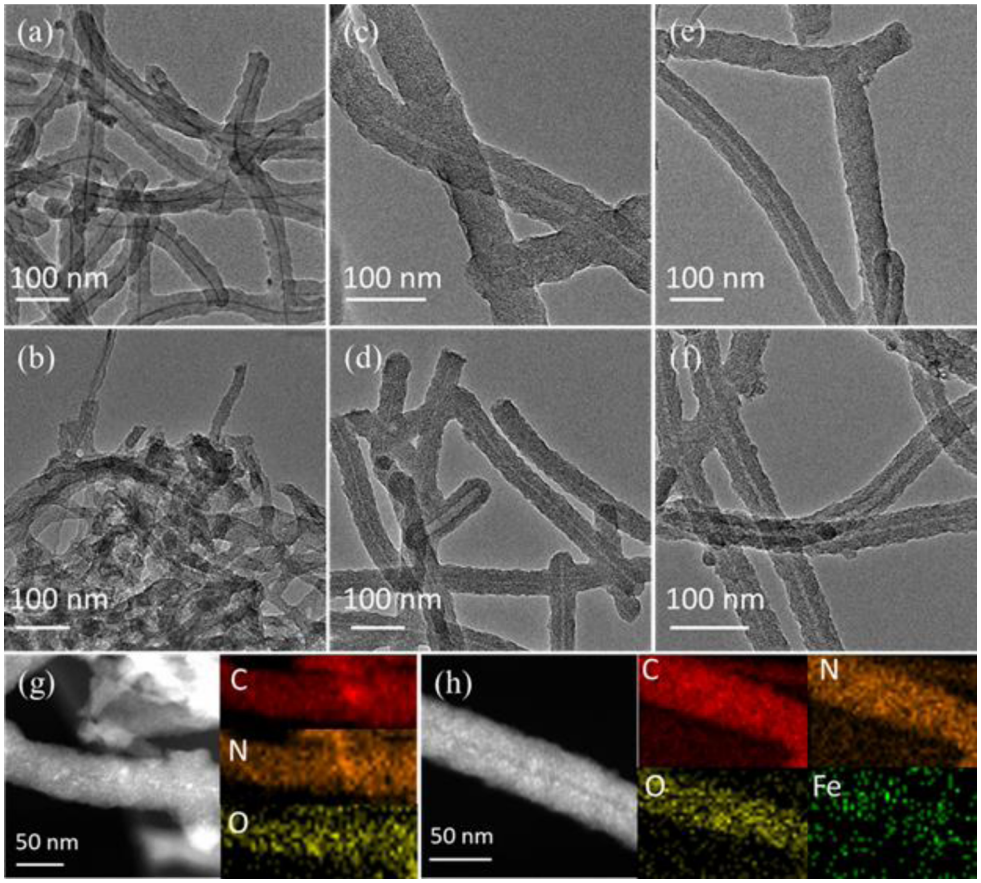

Figure 1. Representative TEM images of (a) Te-MF, (b) MF-900, (c) MF-Fe-600, (d) MF-Fe-700, (e) MF-Fe-800, and (f) MF-Fe-900. HAADF-STEM and elemental mapping images of (g) MF-900 and (h) MF-Fe-800.

Computational Methods. DFT calculations were performed with the open-source planewave code, Quantum Espresso.[53] A two-dimensional supercell was built based on a 6 × 6 unit cell. The vacuum thickness was set at about 14 Å to avoid interactions between periodic images. The ultrasoft pseudopotential[54] was adopted with the kinetic cutoff energy of 40 Ry (charge density cutoff 200 Ry), and 4 × 4 × 1 Monkhorst–Pack K-point grids were sampled for the supercell to converge the total energy to the accuracy of 1 meV. The Marzari–Vanderbilt smearing[55] was adopted with a smearing of 0.002 Ry. The electronic energy was converged to 10^{-8} Ry, and the force was converged to 10^{-4} a.u. Density functional perturbation theory (DFPT)[56] was employed to compute the vibrational frequencies of surface species and molecules for the zero point energy (ZPE) and entropy contribution, similar to a previous work.[57] The implicit solvation calculations were performed with the newly developed solvation model (CANDLE),[58] which has been shown to be suitable for various surfaces in open source code JDFTx.[59,60]

■ RESULTS AND DISCUSSION

In the present study, Te NWs were synthesized by a facile hydrothermal method and used as the structural templates for the synthesis of Fe,N-codoped porous carbon nanotubules. This mainly involved two steps: (a) polymerization of melamine and formaldehyde at 90 °C in the presence of Te NWs led to the deposition of the polymers on the nanowire surface, forming core–sheath nanofibers (Te-MF); and (b) pyrolysis of the obtained Te-MF nanofibers at controlled temperatures, with the addition of a calculated amount of $FeCl_3$ as activating reagent, produced Fe,N-codoped porous carbon nanotubules (MF-Fe-T). In this procedure, melamine was selected as the carbon and nitrogen sources, and formaldehyde was chosen as a second carbon source and linking agent. The structures of the produced carbon nanotubules were first characterized by TEM measurements. Figure 1a depicts a representative TEM image of the Te-MF nanofiber precursors, where the core–sheath structures can be clearly observed. The nanofibers exhibited a length of several hundred nanometers and a diameter of 35–40 nm, and formed a three-dimensional network structure. In addition, the diameter of the Te nanowires can be identified at 5–10 nm. No well-defined lattice fringes were observed in high-resolution TEM measurements (Figure S1a), which indicated the amorphous nature of the melamine–formaldehyde polymer. After pyrolysis at 900 °C, although the fibrous structures were retained, the dark-contrast tellurium nanowires vanished altogether, which led to the formation of a hollow nanotubular structure (MF-900) with the inner diameter consistent with that of the original Te NWs, as shown in Figure 1b. This may be ascribed to the thermal evaporation of the tellurium templates at elevated temperatures. Because of their large atomic radius, the evaporation of the tellurium nanowires might facilitate the formation of a porous structure of the carbon nanotubules and hence a high surface area. Consistent hollow nanotubular structures were obtained when a calculated amount of $FeCl_3$ was mixed with Te-MF prior to pyrolysis at various temperatures (600–900 °C), as manifested in Figure 1c–f for the MF-Fe-T series.

The elemental compositions of the hollow nanotubules were then examined by high angle annular dark field scanning transmission electron microscopy (HAADF-STEM) measurements and elemental mapping analysis. From Figure 1g, one

DOI: 10.1021/acs.chemmater.7b01265
Chem. Mater. 2017, 29, 5617–5628

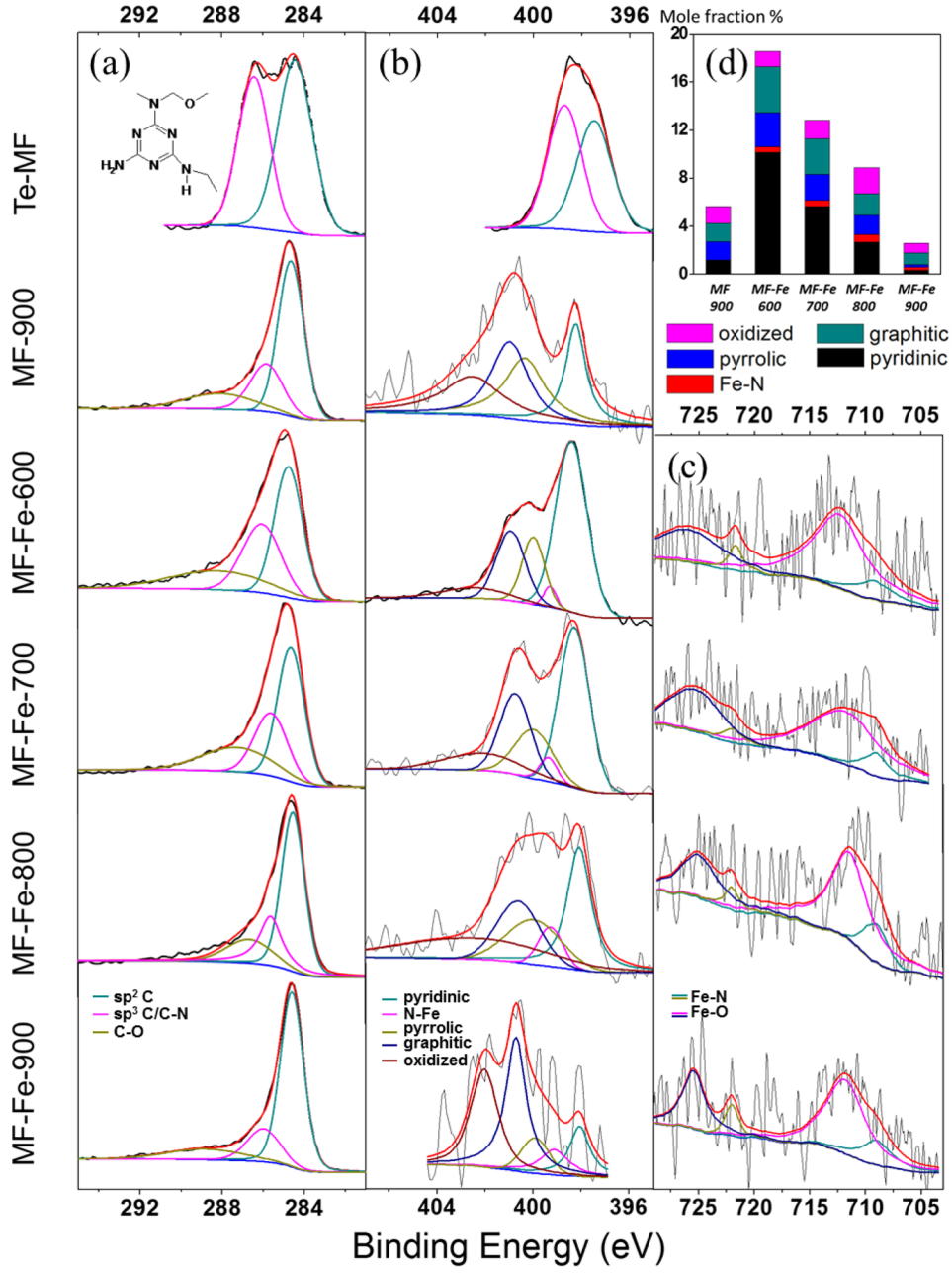

Figure 2. High-resolution XPS scans of (a) C 1s, (b) N 1s, and (C) Fe 2p electrons in the series of nanofiber precursors and doped carbon nanotubules. Gray curves are experimental data, and colored curves are deconvolution fits. (d) Content distributions of various types of nitrogen dopants in the samples. Inset to the top of panel a represents a possible structure of the melamine–formaldehyde resin, where the amino group of melamine is linked to $-CH_2-O-CH_2-$, $-CH_2-$, or free.

can see that in the MF-900 sample, the elements of carbon, nitrogen, and oxygen were all readily identified and distributed rather homogeneously throughout the nanotubules, which suggested the formation of nitrogen-doped carbons. When pyrolysis of Te-MF was carried out in the presence of $FeCl_3$, in addition to carbon, nitrogen, and oxygen, the Fe signals were also found across the nanotubules, as exemplified by the MF-Fe-800 sample (Figure 1h). This suggests that both nitrogen and iron were doped into the carbon molecular skeletons.

The elemental compositions and valence states were then examined by XPS measurements. From the survey spectra in Figure S2, one can see that both Te-MF and MF-900 samples exhibited three well-defined peaks at 285, 400, and 531 eV, which may be ascribed to the C 1s, N 1s, and O 1s electrons, respectively. For the MF-Fe-T series (T = 600, 700, 800, and 900) of Fe,N-codoped carbon nanotubules, the Fe 2p electrons can also be identified at ~710 eV. The high-resolution scans of the C 1s electrons were depicted in Figure 2a. One can see that deconvolution of the Te-MF spectrum yields two peaks at 284.43 and 286.43 eV due to the sp^2 and sp^3 C in the melamine–formaldehyde polymer (Figure 2a inset), respectively.[61] After pyrolysis at elevated temperatures, all samples exhibited a major C 1s peak at ~284.6 eV, which can be assigned to graphitic sp^2 C, signifying successful carbonization of the melamine-formaldehyde polymer at elevated temperatures, despite the lack of long-range lattice fringes in high-resolution TEM measurements (Figure S1b–f).[62] There are also two minor peaks at 285.6–286.0 eV and 286.6–288.0 eV.

DOI: 10.1021/acs.chemmater.7b01265
Chem. Mater. 2017, 29, 5617–5628

The former is most likely due to the combined contributions of sp^3 carbon and N-bonded carbon (Figure 2a inset),[62−64] whereas the latter may be ascribed to oxidized carbon. Notably, on the basis of the integrated peak areas, the content of graphitic sp^2 C was found to increase markedly with pyrolysis temperature (Table S1), 38.2% for MF-Fe-600, 42.1% for MF-Fe-700, 52.7% for MF-Fe-800, and 66.6% for MF-Fe-900, indicating enhanced graphitization of the polymer precursors (for the minor carbon species, the contents were much lower at 10−20%). For comparison, the content of graphite sp^2 C for MF-900 (56.2%) was lower than that of MF-Fe-900, which might be ascribed to the promoting effect of Fe species in the formation of graphitic carbons.[40,65]

The N 1s spectra are depicted in Figure 2b. For Te-MF, two peaks were resolved at 397.5 and 398.7 eV at almost equal concentration and may be assigned to the sp^2 N in C═N and sp^3 N in N−H (Figure 2a inset), respectively. By contrast, deconvolution of the MF-900 spectrum yielded four nitrogen species at 398.24, 400.35, 401.00, and 402.55 eV, consistent with the binding energies of pyridinic, pyrrolic, graphitic, and oxidized nitrogens, respectively,[66] indicating that nitrogen was indeed incorporated into the graphitic molecular skeletons by high-temperature pyrolysis. For the series of MF-Fe-T samples, these four types of nitrogen dopants remained well resolved at consistent binding energies. Furthermore, one additional nitrogen species may be resolved at 399.3 eV, which can be ascribed to N in Fe−N moieties.[29,35,40,67] The nitrogen contents were then quantified, where one can see that the overall nitrogen concentration decreased with increasing pyrolysis temperature (Table S1), 18.5 at% for MF-Fe-600, 12.9 at% for MF-Fe-700, 8.9 at% for MF-Fe-800, and 2.6 at% for MF-Fe-900 (note that it was somewhat higher at 5.6 at% for MF-900). Figure 2d depicts the concentrations of the various nitrogen dopants within each sample. One can see that pyridinic nitrogen accounted for ∼50% of the nitrogen dopants in the MF-Fe-600 and MF-Fe-700 samples, but for the samples prepared at higher temperatures (MF-Fe-800 and MF-Fe-900), (oxidized) graphitic nitrogen became the dominant species, indicating enhanced thermal stability of the latter as compared to the former (Table S2).[68]

The Fe 2p data are depicted in Figure 2c. One can see that the series of MF-Fe-T samples all exhibited two pairs of peaks. The first doublet can be identified at ∼709 and 722 eV, most likely due to Fe atoms bonded to N,[67,69] whereas the other at ∼712 and 725 eV arose from Fe in iron oxides such as Fe_3O_4, Fe_2O_3, and Fe−O−C.[70,71] Notably, the total Fe content was found to be ∼1 at%, increasing slightly from 0.81% for MF-Fe-600 to 0.92% for MF-Fe-700, reaching a maximum at 1.01% for MF-Fe-800, but then diminishing to 0.68% for MF-Fe-900 (Table S1), most probably due to the thermal volatility of the iron species at elevated temperatures.[40,65] Remarkably, the atomic ratio of Fe and N in Fe−N bonds was found to be 4.0 for MF-Fe-600, MF-Fe-700, and MF-Fe-800, but only 1.67 for MF-Fe-900, indicating the formation of FeN_4 moieties in the first three samples whereas in the last one, Fe was highly undercoordinated probably because of the low overall concentration of the nitrogen dopants (Table S1).

Further structural insights were obtained in Raman measurements. Figure 3 depicts the Raman spectra of the series of carbon nanotubules, which all exhibited a well-defined D band at ∼1350 cm^{-1} and a G band at ∼1577 cm^{-1}, again, confirming the formation of graphitic carbons by pyrolysis of the polymer precursors. In addition, one can see that the ratio of the D and G band intensity decreased slightly with increasing pyrolysis temperature, at 2.93 for MF-Fe-600, 2.77 for MF-Fe-700, and 2.57 for MF-Fe-800, but then increased somewhat to 2.95 for MF-Fe-900 (Table S3), indicating an initial increase of the degree graphitization with pyrolysis temperature; yet at too high of a temperature, the porous graphitic framework might collapse, leading to the formation of an increasingly defective structure. That is, within the present experimental context, 800 °C represented an optimal pyrolysis temperature, corresponding to the lowest concentration of structural defects in the resulting hollow carbon nanotubules.

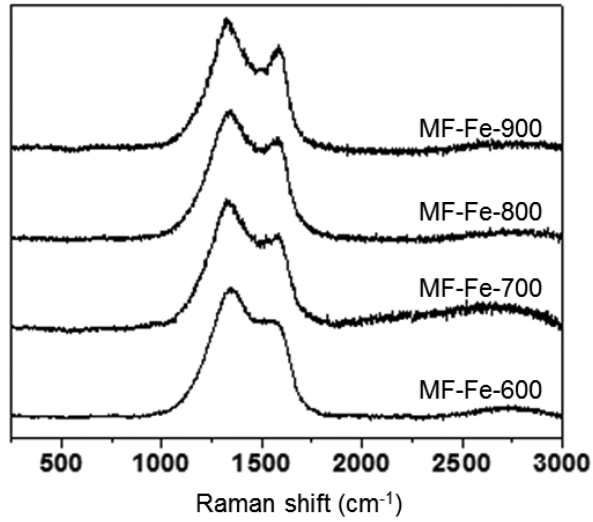

Figure 3. Raman spectra of the Fe,N-codoped carbon (MF-Fe-T) nanotubules.

Significantly, the obtained doped carbon nanotubules exhibited apparent electrocatalytic activity toward ORR. Figure 4a depicts the RRDE voltammograms of a glassy carbon electrode modified with a calculated amount of the carbon nanotubules prepared above. One can see that as the electrode potential was swept negatively, nonzero current started to emerge, indicating oxygen reduction catalyzed by these doped carbon nanotubules. Yet, a closer analysis shows that the performance actually varied among the series of samples. For instance, the onset potential (E_{onset}) was found to increase in the order of MF-900 (+0.85 V) < MF-Fe-600 (+0.86 V) < MF-Fe-700 (+0.92 V) < MF-Fe-900 (+0.97 V) < MF-Fe-800 (+0.98 V). These are also summarized in Table 1 (a similar variation can also be observed with the half-wave potential, $E_{1/2}$). In fact, the onset potential of MF-Fe-800 was even slightly more positive than that (+0.97 V) of commercial Pt/C. In addition, one can see that the onset potential of MF-900 was comparable to that of metal-free carbon catalysts for ORR reported in the literature;[72−74] however, the fact that it was markedly more negative than those of the MF-Fe-T series indicates the significant role of Fe dopants (most likely FeN_4 moieties) in the enhancement of the ORR performance, as detailed below.

Furthermore, one can see that all carbon nanotubule catalysts showed a very low ring current density with the ring potential set at +1.5 V, indicating the production of only a minimal amount of peroxide species during oxygen reduction. This is clearly illustrated in Figure 4b, which shows the number of electron transfer (n) involved in ORR within the potential range of +1.0 to +0.2 V, with $n = \frac{4I_{Disk}}{I_{Disk} + I_{Ring}/N}$, where I_{Disk} and

DOI: 10.1021/acs.chemmater.7b01265
Chem. Mater. 2017, 29, 5617−5628

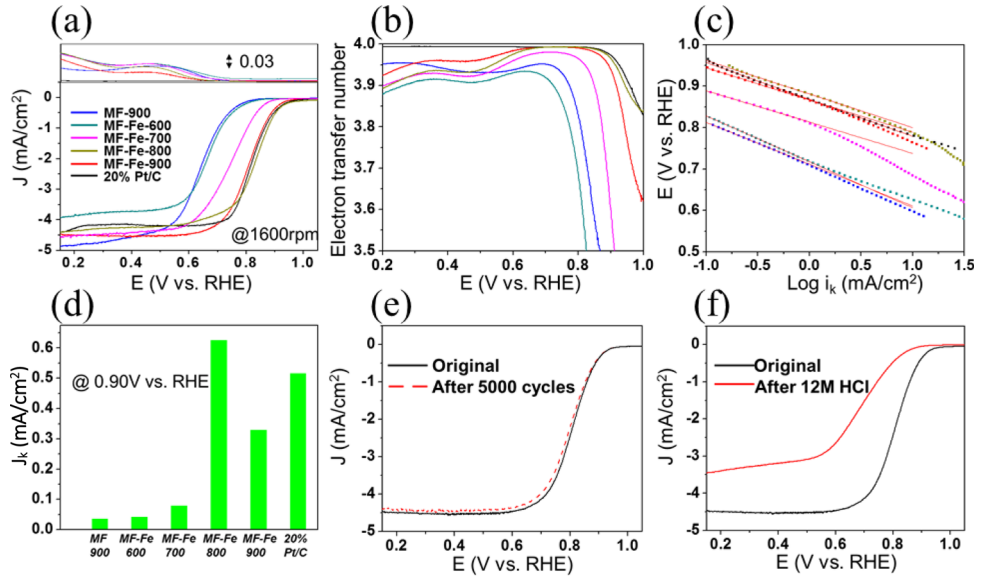

Figure 4. ORR performance of N and Fe,N-doped carbon nanofibers. (a) RRDE voltammograms at the rotation rate of 1600 rpm and potential scan rate of 10 mV/s in an oxygen-saturated 0.1 M KOH solution. The upper panel is ring current density with a scale bar at 0.03 mA/cm^2, and the lower panel is current density. (b) Variation of the number of electron transfer (n) with electrode potential. (c) Tafel plot for the series of samples. The legends of panels b and c are the same as those in panel a. (d) Comparison of the kinetic current density at +0.9 V versus RHE. (e) RDE voltammograms of MF-Fe-800 before and after 5000 cycles of potential scans at the scan rate of 500 mV/s. (f) RDE voltammograms of MF-Fe-800 before and after acid etching with 12 M HCl.

Table 1. Summary of ORR Performance of the Series of Carbon Nanotubules

sample	E_{onset} (V vs RHE)	$E_{1/2}$ (V vs RHE)	n at +0.7 V	J_k at +0.9 V (mA/cm^2)	Tafel slope (mV/dec)
MF-900	0.85	0.64	3.95	0.05	101
MF-Fe-600	0.86	0.67	3.92	0.05	111
MF-Fe-700	0.92	0.75	3.98	0.08	76
MF-Fe-800	0.98	0.83	3.99	0.63	81
MF-Fe-900	0.97	0.81	3.99	0.33	78
20% Pt/C	0.97	0.82	3.99	0.53	89

I_{Ring} are the voltammetric currents at the disk and ring electrodes, respectively, and N is the collection efficiency (40%).[75] One can see that at all samples, the n values are over 3.9, indicating almost complete reduction of oxygen to OH^- through the four-electron pathway. Yet, small discrepancy can be observed. For instance, at +0.70 V, n increased slightly in the order of MF-Fe-600 (3.92) < MF-Fe-700 (3.98) < MF-Fe-900 ≈ MF-Fe-800 ≈ Pt/C (3.99), as shown in Table 1.

Further comparison can be made with the Tafel plots (Figure 4c). One can see that the kinetic current density increased with increasing overpotentials, and within the wide range of electrode potential from +1.0 to +0.6 V, the MF-Fe-800 sample exhibited the highest kinetic current density among the series. For instance, at +0.90 V, the kinetic current density was found to be less than 0.05 mA/cm^2 for MF-900 and MF-Fe-600, 0.08 mA/cm^2 for MF-Fe-700, 0.63 mA/cm^2 for MF-Fe-800, and 0.33 mA/cm^2 for MF-Fe-900 (Figure 4d). Significantly, the performance of MF-Fe-800 was even better

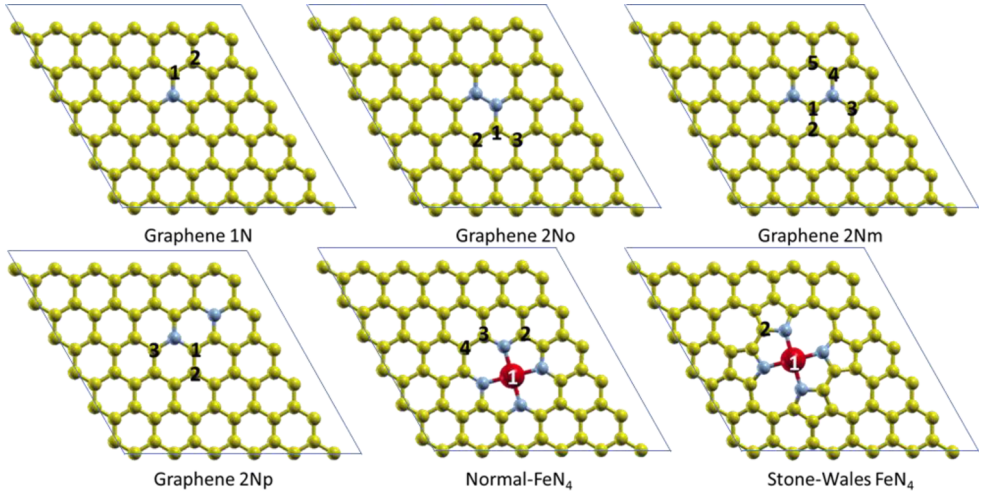

Figure 5. Atomistic models of N and FeN_4-doped graphene. The numbers indicate tested candidate active sites for ORR activity. Atoms are shown as blue (N), red (Fe), and yellow (C) spheres.

DOI: 10.1021/acs.chemmater.7b01265
Chem. Mater. 2017, 29, 5617−5628

than that of Pt/C (0.53 mA/cm^2). Furthermore, the Tafel slope may also be quantified and compared, which was 101 mV/dec for MF-900 and 111 mV/dec for MF-Fe-600, but decreased markedly to 76 mV/dec for MF-Fe-700, 81 mV/dec for MF-Fe-800 and 78 mV/dec for MF-Fe-900, all close to that of (89 mV/dec) for commercial Pt/C (Table 1). This suggests that with increasing pyrolysis temperature, the resulting Fe,N-codoped carbon nanotubules behaved analogously to Pt/C, where the rate-determining step was likely the first electron-reduction of oxygen.

The series of MF-Fe-T catalysts also showed excellent durability. Take MF-Fe-800 as the example, $E_{1/2}$ exhibited a negative shift of less than 7 mV after 5000 cycles of potential scans (Figure 4e). In addition, after the carbon nanotubules were subject to chemical etching with 12 M HCl, one can see that the activity diminished markedly, with a negative shift of about 100 mV of the onset potential and a 30% decrease of the limiting currents (Figure 4f). These observations indicate that Fe species played an indispensable role in the ORR activity, most likely through the FeN_4 moieties in the Fe,N-codoped carbon nanotubules. Such a remarkable performance is highly comparable or even superior to leading results reported in recent literature with relevant carbon-based catalysts (Table S4).

Taken together, these experimental results indicate that the MF-Fe-800 sample stood out as the best catalyst among the series. In addition, although apparent ORR activity was observed with carbons doped with nitrogen alone, the performance was markedly improved with additional doping of Fe-containing compounds. That is, the Fe species, rather than the N dopants, played a dominant role in determining the ORR activity.

First-principles calculations were then carried out to shed light on the contributions of nitrogen dopants and FeN_4 moieties to the electrocatalytic activity. It was observed that pyrrolic and oxidized nitrogen dopants had only minimal contributions to the ORR activity, and pyridinic nitrogen was mostly inactive in binding oxygeneous species (Figure S3), consistent with earlier results.[36,42,76] Therefore, the calculations were focused mainly on graphitic nitrogen dopants and FeN_4 moieties, with several representative models depicted in Figure 5, which were based upon experimental data presented above in Figure 2 and Table S1. For the graphitic nitrogen, two scenarios were examined: (a) one isolated N dopant in the graphene supercells such that there is no interaction between the N dopants (Graphene 1N, Figure 5), and (b) two N dopants in the same hexatomic ring in the supercell, where interactions between the two N dopants are possible (only negligible interactions between N dopants from different hexatomic rings), at three different configurations, the ortho (Grapnene 2No, Figure 5), meso (Grapnene 2 Nm, Figure 5), and para (Grapnene 2 Np, Figure 5) structures. In addition, as XPS studies suggest the formation of FeN_4 moieties in the carbon structure, two FeN_4 doped graphene structures were also studied with the normal FeN_4 and Stone–Wales defect FeN_4 (Figure 5).[77−79]

In the electrochemical measurements (Figure 4), the n values were found to be close to 4, indicating that the ORR process mostly followed the four-electron reduction pathway, which involves the following steps:

$$* + O_2 + H^+ + e^- \rightarrow OOH^* \quad \Delta G_1 \tag{1}$$

$$OOH^* + H^+ + e^- \rightarrow O^* + H_2O \quad \Delta G_2 \tag{2}$$

$$O^* + H^+ + e^- \rightarrow OH^* \quad \Delta G_3 \tag{3}$$

$$OH^* + H^+ + e^- \rightarrow H_2O + * \quad \Delta G_4 \tag{4}$$

where $*$ is the active site, and the ORR activity has been argued to be most likely limited by two reactions, the first electron reduction of oxygen (eq 1) and reduction of adsorbed hydroxy to water and its desorption from the catalyst surface (eq 4).[12,42,80] That is, the binding of the catalytic active sites to oxygen species cannot be too strong or too weak. In fact, within this mechanistic model, the overall reaction will be optimized with a smallest reaction free energy of the limiting step when $\Delta G_1 = \Delta G_4$. As $\Delta G_2 + \Delta G_3 = \Delta E_{OH^*} - \Delta E_{OOH^*}$ (where ΔG is reaction free energy and ΔE is adsorption energy), and based on the Faraday's law, the total energy $\Delta G^\circ = \Sigma \Delta G_i = -4E^\circ = -4.92$ eV with E° being the formal potential (+1.23 V) of oxygen reduction. Thus, the smallest possible free energy for reactions 1 and 4 is $\Delta G_{ave} = \Delta G_1 = \Delta G_4 = 1/2(\Delta G_1 + \Delta G_4) = 1/2[\Delta G^\circ - (\Delta E_{OH^*} - \Delta E_{OOH^*})]$. It has been observed that there is a linear relationship between ΔE_{OOH^*} and ΔE_{OH^*}. Thus, $\Delta E_{OOH^*} - \Delta E_{OH^*}$ is a constant, which is defined as b, and the optimal potential is obtained as

$$U = -\Delta G_{ava}/2e = -(-4.92 + b)/2 \tag{5}$$

Figure 6 depicts the linear relationship between the calculated binding energies of OOH and OH intermediates at the various carbon active sites, including carbon atoms in the FeN_4 structures (Figure 5). Linear regression yields a slope of 1.03, which is only within 3% of the theoretical value of 1, and the intercept of 3.24 eV is in the typical range of 3.0−3.4 eV that has been observed previously.[80,81] From eq 5, the optimal potential for the carbon sites was estimated to be 0.84 V, in good agreement with the experimental onset potential of 0.85 eV observed above for nitrogen-doped carbon, MF-900. Notably, one can see from Figure 6 that for both FeN_4

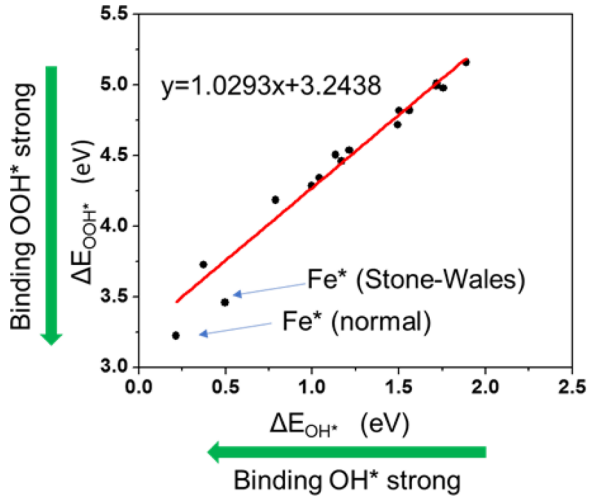

Figure 6. Correlation between the adsorption energies of the OOH and OH intermediate species. The two data points at the bottom are for the Fe sites in Normal FeN_4 and Stone−Wales FeN_4 as showed in Figure 5. Other data points represent results for the various carbon sites from the structures shown in Figure 5, and the red line is the linear regression of these data. The green arrows indicate the direction of increasing binding energies.

DOI: 10.1021/acs.chemmater.7b01265
Chem. Mater. 2017, 29, 5617−5628

structures (Figure 5) the iron centers have a more optimal potential than the carbon sites. Using a slope of 1, we estimated the intercepts of 3.01 eV for Fe in the normal FeN_4 structure and 2.96 eV for Fe in the Stone−Wales FeN_4 structure. Thus, from eq 5, the corresponding optimal potentials can be estimated to be 0.96 and 0.98 V for these Fe−N codoped structures, in excellent agreement with the experimental onset potential (+0.98 V) observed for Fe,N-codoped carbon nanotubules, MF-Fe-800 (Figure 4). This strongly suggests that indeed the Fe centers played a more significant role in determining the ORR than the carbon sites, as the theoretical onset potential of the latter is 120−140 mV more positive than that of the former (Table 1).

It should be noted that in the above calculations the following two factors are neglected: (a) reactions 1 and 4 are assumed to be the rate-determining steps with the activity optimized at $\Delta G_1 = \Delta G_4$. However, this ideal situation is difficult to reach, as step (3) is also an "uphill" reaction and may be involved in controlling the overall reaction kinetics; and (b) the ZPE correction, entropy correction, and solvation energy correction were ignored. Thus, to make more accurate predictions and correlations with experimental data, we carefully calculated all four steps of ORR reactions for each candidate active site at the potential at +0.9 V versus RHE. ZPE correction, entropy correction, and solvation energy corrections were all included in the reaction free energy calculations, as showed explicitly in Table S5 and graphically in Figures 7 and

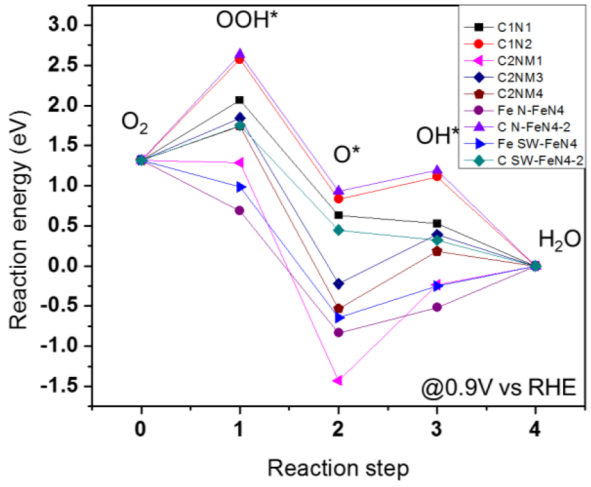

Figure 7. Reaction free energy diagram of reaction steps (1)−(4) in ORR at the various atomistic sites that are defined in Figure 5. In the figure legends, C1N1 and C1N2 refer to the C1 and C2 sites in Graphene 1N, respectively. C2NM1, C2NM3, and C2NM4 refer to the C1, C3, and C4 sites in Graphene 2Nm, respectively. Fe N-FeN4 and C N-FeN4−2 refer to the Fe site and C2 site in normal-FeN_4, respectively. Fe SW-FeN4 and C SW-FeN4−2 refer to the Fe site and C2 site in Stone−Wales FeN_4, respectively.

S4. It can be seen that nearly all carbon sites showed a very high ΔG_1, signifying that carbon sites experienced difficulty in adsorbing OOH* intermediate. In addition, although at some sites the third step showed the highest energies, the first step remained energetically unfavorable. Correspondingly, the reaction energy of the last step on all carbon sites was negative, suggesting that the OH species might be easily released from the carbon sites. On the contrary, for the Fe sites in the FeN_4 structures, step (3) or (4) can be identified as the rate-determining step, signifying favorable binding with oxygen species. Hence, adsorption of O_2 is energetically favorable, while the release of OH is unfavorable, consistent with results from recent studies.[82] From Table S5, one can also see that the most active structures are Graphene 2 Nm-3, where the two nitrogen dopants are in a meso configuration, with a reaction free energy of the limiting step of only 0.61 eV; such a number diminished further to 0.51 eV for the Fe sites of normal FeN_4 and 0.39 eV for Stone−Wales FeN_4. From these calculations, we can then estimate the minimal reaction current density:

$$J = J_o e^{-\Delta G/k_B T} \tag{6}$$

where J is the current density, k_B is the Boltzmann constant, and T is temperature.[80] Thus, the ratio between the current density of the Fe,N-codoped graphene over N-doped graphene can be estimated to be

$$\frac{J_{Fe,N}}{J_N} = e^{-\Delta G_{Fe,N-max} + \Delta G_{N-min}/k_B T} \tag{7}$$

where $\Delta G_{Fe,N\text{-}max}$ and $\Delta G_{N\text{-}min}$ denote the largest free energy of Fe sites and lowest free energy of N-doped C sites. At room temperature (298 K), this current density ratio was estimated to be 36.14, implying that the Fe sites of FeN_4 in Fe,N-codpoed carbons are over 36-times more active than carbon with N doping alone. Experimentally, the kinetic current density of MF-Fe-800 was calculated to be about 20-times higher than that of MF-900 (Figure 4 and Table 1), in rather good agreement with this theoretical prediction.

Furthermore, from Table S5, one can see that the carbon atoms adjacent to a nitrogen dopant are more active than the next nearest neighbors. For example, the nearest-neighbor carbons in Graphene 1N-1, 2No-1, 2Nm-3, 2Nm-4, 2Np-1, and 2Np-3 (Figure 5) exhibited a reaction free energy of the limiting step of 0.75, 0.67, 0.61, 0.71, 0.78, and 0.78 eV, respectively, all much lower than those in the second nearest neighbor configurations, Graphene 1N-2 (1.25 eV), 2No-2 (1.06 eV), 2Nm-2 (0.96 eV), 2Nm-5 (1.06 eV), and 2Np-2 (1.22 eV), consistent with results reported previously.[83] Note that the carbon site of Stone−Wales FeN_4 exhibited a reaction free energy of the limiting step of only 0.43 eV, much lower than those of carbon sites in other configurations. This indicates that some carbon atoms can also contribute to the activity in Fe,N-codoped graphene. In fact, in a previous study,[40] we observed that despite a low Fe concentration (~1%), Fe,N-codoped carbon exhibited a remarkable ORR activity.

We selected two representative systems, Graphene 2Nm and Normal FeN_4 (Figure 5), for a more comprehensive study of their electronic structures to identify the critical factors that determine the different activities between Fe,N-codoped graphene and N-doped graphene. From the reaction free energy calculations of these systems (Figure 7), one can see that it is difficult for carbon to adsorb oxygen species in N-doped graphene, while it is much easier for Fe in FeN_4-doped graphene. In fact, the binding of oxygen is more favorable when a high density of states exists right below the Fermi level. For example, we plotted both the total density of states (DOS) along with the projected density of states of potentially active sites in Figure 8 to determine which atoms have states near the Fermi level. For the N-doped graphene system, the carbon atoms that are nearest to nitrogen contributed the most to the DOS near the Fermi level. However, their DOS near the Fermi

DOI: 10.1021/acs.chemmater.7b01265
Chem. Mater. 2017, 29, 5617−5628

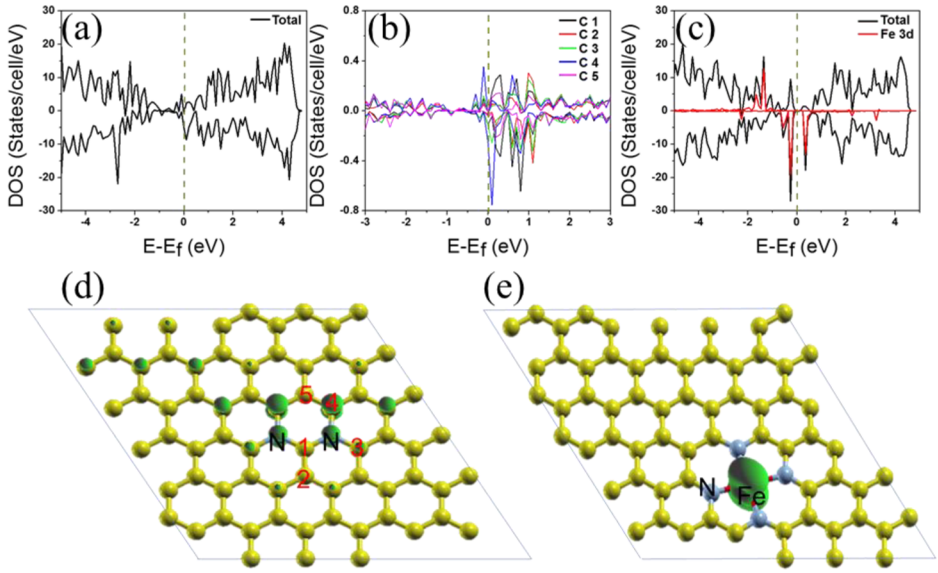

Figure 8. Density of state (DOS), projected density of states, and spin density distribution in N-doped and FeN_4-doped graphene systems. DOS plots of (a) Graphene 2N m; (b) zoomed-in around the Fermi level of panel a showing the DOS contribution of various carbon sites (Figure 5); and (c) normal FeN_4. The yellow broken line shows the location of the Fermi level. Spin density distribution plots of (d) Graphene 2Nm and (e) normal FeN_4. The green isosurface is the unpaired electron distribution (spin up-spin down). The isovalue is the same at 0.004 e/au^3 for panels d and e.

level (Figure 8b) is still much smaller than that of FeN_4 (Figure 8c), indicating a lower probability to donate electrons and reduce O_2. Moreover, although carbon sites 3 and 4 had the largest contributions to the states, none of them had a dominant contribution (projected DOS in Figure 8b). From Figure 8c, we see that FeN_4 has one order of magnitude higher density of state below the Fermi level composed predominantly of the Fe 3d orbitals.

Furthermore, it can be found that the spin density is also critical to the ORR activity because the atoms with unpaired spins have radical characters, which are highly reactive and may easily attack O_2 molecules. Figure 8d and e depict the spin density distributions. Since Fe takes a high spin configuration in FeN_4, it has a large distribution in the spin density plot from its unpaired 3d orbitals. Meanwhile, the carbon near nitrogen (along with the nitrogen itself) is shown to have some unpaired electron distribution as well. Yet the spin density distribution on carbon is clearly less than the dominating cloud associated with Fe. Therefore, Fe's unpaired 3d orbitals along with their position near the Fermi level may explain why iron binds so favorably to oxygen species. This also coincides with results in a previous study,[77] where the Fe 3d unpaired electrons may cause strong interactions with O_2 for the initial step of ORR. On the contrary, we see the opposite for N, that is, there are fewer states near the Fermi level and a much smaller distribution of unpaired electrons in N-doped graphene. In fact, from Table S6, one can see that the active sites have higher unpaired spin: in N-doped graphene, only the C atoms with unpaired spins (small compared with Fe) are active (site 3 and 4), whereas in Fe,N-codoped graphene, Fe has nearly two unpaired spins leading to a highly active site.

CONCLUSION

Nitrogen and iron codoped carbon hollow nanotubules were synthesized by controlled pyrolysis of core−sheath nanofibers based on Te NWs-supported melamine formaldehyde polymer with the addition of a calculated amount of $FeCl_3$, where the Te NWs served as thermally removable templates because of its low boiling point. Electron microscopic and XPS measurements confirmed the successful incorporation of Fe and N dopants into the carbon molecular skeletons, and electrochemical studies of the resulting nanocomposites showed apparent activity toward ORR in alkaline media that was highly comparable to leading results reported in recent literature, within the context of onset potential, number of electron transfer, and kinetic current density. Significantly, the sample prepared at 800 °C stood out as the best catalysts among the series, with a performance even better than that of commercial Pt/C. In addition, comparative studies with N-doped carbons prepared in a similar fashion suggested that Fe species, rather than nitrogen dopants, played a dominant role in dictating the ORR activity, most probably due to the formation of FeN_4 moieties. This was further supported by first-principles calculations where the atomistic models were built based on the structural characteristics obtained in experimental studies. Theoretically, the optimal potential for the Fe sites was 120−140 mV more positive than that of N-doped carbon sites and correlated well with the ORR onset potentials observed experimentally. Notably, the limited activity of N-doped carbon was ascribed to the low binding of oxygeneous species, as suggested by the low DOS below the Fermi level and low spin density; in contrast, the Fe sites of the FeN_4 structure were far more active in the adsorption of oxygen intermediates, in excellent agreement with experimental results. From the combined experimental and theoretical studies, one can see that Fe species, in particular, FeN_4 moieties, likely played a dominant role in the determination of the ORR activity. This may be exploited as a fundamental framework for the rational design of high-performance ORR catalysts by deliberate engineering of the nanocomposite structures.

ASSOCIATED CONTENT

Supporting Information

The Supporting Information is available free of charge on the ACS Publications website at DOI: 10.1021/acs.chemmater.7b01265.

DOI: 10.1021/acs.chemmater.7b01265
Chem. Mater. 2017, 29, 5617−5628

Additional experimental data and discussion (PDF)

AUTHOR INFORMATION

Corresponding Authors

*E-mail: shaowei@ucsc.edu.
*E-mail: yuanping@ucsc.edu.

ORCID

Dongdong Qin: 0000-0002-8927-8601
Shaowei Chen: 0000-0002-3668-8551

Author Contributions

The manuscript was written through contributions of all authors. All authors have given approval to the final version of the manuscript.

Notes

The authors declare no competing financial interest.

ACKNOWLEDGMENTS

This work was supported, in part, by the National Science (DMR-1409396). TEM was carried out at Lanzhou Institute of Chemical Physics, Chinese Academy of Sciences. XPS work was carried out at the Molecular Foundry of the Lawrence Berkeley National Laboratory. This work used the Extreme Science and Engineering Discovery Environment (XSEDE), which is supported by the National Science Foundation (ACI-1548562).[84] We thank Prof. J. Z. Zhang and A. Allen for the acquisition of the Raman spectra.

REFERENCES

(1) Green, M. A.; Bremner, S. P. Energy conversion approaches and materials for high-efficiency photovoltaics. *Nat. Mater.* **2016**, *16*, 23−34.
(2) Stamenkovic, V. R.; Strmcnik, D.; Lopes, P. P.; Markovic, N. M. Energy and fuels from electrochemical interfaces. *Nat. Mater.* **2016**, *16*, 57−69.
(3) Dusastre, V.; Martiradonna, L. Materials for sustainable energy. *Nat. Mater.* **2016**, *16*, 15−15.
(4) Ping, Y.; Goddard, W. A., 3rd; Galli, G. A. Energetics and Solvation Effects at the Photoanode/Catalyst Interface: Ohmic Contact versus Schottky Barrier. *J. Am. Chem. Soc.* **2015**, *137*, 5264−7.
(5) Wang, Y. J.; Qiao, J.; Baker, R.; Zhang, J. Alkaline polymer electrolyte membranes for fuel cell applications. *Chem. Soc. Rev.* **2013**, *42*, 5768−87.
(6) Zhang, H.; Shen, P. K. Recent development of polymer electrolyte membranes for fuel cells. *Chem. Rev.* **2012**, *112*, 2780−832.
(7) Li, M.; Zhao, Z.; Cheng, T.; Fortunelli, A.; Chen, C. Y.; Yu, R.; Zhang, Q.; Gu, L.; Merinov, B. V.; Lin, Z.; Zhu, E.; Yu, T.; Jia, Q.; Guo, J.; Zhang, L.; Goddard, W. A., 3rd; Huang, Y.; Duan, X. Ultrafine jagged platinum nanowires enable ultrahigh mass activity for the oxygen reduction reaction. *Science* **2016**, *354*, 1414−1419.
(8) Huang, X.; Zhao, Z.; Cao, L.; Chen, Y.; Zhu, E.; Lin, Z.; Li, M.; Yan, A.; Zettl, A.; Wang, Y. M.; Duan, X.; Mueller, T.; Huang, Y. ELECTROCHEMISTRY. High-performance transition metal-doped Pt(3)Ni octahedra for oxygen reduction reaction. *Science* **2015**, *348*, 1230−4.
(9) Bu, L.; Zhang, N.; Guo, S.; Zhang, X.; Li, J.; Yao, J.; Wu, T.; Lu, G.; Ma, J. Y.; Su, D.; Huang, X. Biaxially strained PtPb/Pt core/shell nanoplate boosts oxygen reduction catalysis. *Science* **2016**, *354*, 1410−1414.
(10) Zhu, C.; Li, H.; Fu, S.; Du, D.; Lin, Y. Highly efficient nonprecious metal catalysts towards oxygen reduction reaction based on three-dimensional porous carbon nanostructures. *Chem. Soc. Rev.* **2016**, *45*, 517−31.
(11) Zhou, M.; Wang, H. L.; Guo, S. Towards high-efficiency nanoelectrocatalysts for oxygen reduction through engineering advanced carbon nanomaterials. *Chem. Soc. Rev.* **2016**, *45*, 1273−307.
(12) Peng, Y.; Lu, B.; Wang, N.; Li, L.; Chen, S. Impacts of interfacial charge transfer on nanoparticle electrocatalytic activity towards oxygen reduction. *Phys. Chem. Chem. Phys.* **2017**, *19*, 9336−9348.
(13) Hu, P. G.; Liu, K.; Deming, C. P.; Chen, S. W. Multifunctional graphene-based nanostructures for efficient electrocatalytic reduction of oxygen. *J. Chem. Technol. Biotechnol.* **2015**, *90*, 2132−2151.
(14) Gong, K.; Du, F.; Xia, Z.; Durstock, M.; Dai, L. Nitrogen-doped carbon nanotube arrays with high electrocatalytic activity for oxygen reduction. *Science* **2009**, *323*, 760−4.
(15) Zhang, J.; Zhao, Z.; Xia, Z.; Dai, L. A metal-free bifunctional electrocatalyst for oxygen reduction and oxygen evolution reactions. *Nat. Nanotechnol.* **2015**, *10*, 444−52.
(16) Fei, H.; Ye, R.; Ye, G.; Gong, Y.; Peng, Z.; Fan, X.; Samuel, E. L.; Ajayan, P. M.; Tour, J. M. Boron- and nitrogen-doped graphene quantum dots/graphene hybrid nanoplatelets as efficient electrocatalysts for oxygen reduction. *ACS Nano* **2014**, *8*, 10837−43.
(17) Higgins, D. C.; Hoque, M. A.; Hassan, F.; Choi, J. Y.; Kim, B.; Chen, Z. W. Oxygen Reduction on Graphene-Carbon Nanotube Composites Doped Sequentially with Nitrogen and Sulfur. *ACS Catal.* **2014**, *4*, 2734−2740.
(18) Ferrero, G. A.; Preuss, K.; Marinovic, A.; Jorge, A. B.; Mansor, N.; Brett, D. J.; Fuertes, A. B.; Sevilla, M.; Titirici, M. M. Fe-N-Doped Carbon Capsules with Outstanding Electrochemical Performance and Stability for the Oxygen Reduction Reaction in Both Acid and Alkaline Conditions. *ACS Nano* **2016**, *10*, 5922−32.
(19) Shang, L.; Yu, H.; Huang, X.; Bian, T.; Shi, R.; Zhao, Y.; Waterhouse, G. I.; Wu, L. Z.; Tung, C. H.; Zhang, T. Well-Dispersed ZIF-Derived Co,N-Co-doped Carbon Nanoframes through Mesoporous-Silica-Protected Calcination as Efficient Oxygen Reduction Electrocatalysts. *Adv. Mater.* **2016**, *28*, 1668−74.
(20) Ma, N.; Jia, Y.; Yang, X. F.; She, X. L.; Zhang, L. Z.; Peng, Z.; Yao, X. D.; Yang, D. J. Seaweed biomass derived (Ni,Co)/CNT nanoaerogels: efficient bifunctional electrocatalysts for oxygen evolution and reduction reactions. *J. Mater. Chem. A* **2016**, *4*, 6376−6384.
(21) Yu, H.; Fisher, A.; Cheng, D.; Cao, D. Cu,N-codoped Hierarchical Porous Carbons as Electrocatalysts for Oxygen Reduction Reaction. *ACS Appl. Mater. Interfaces* **2016**, *8*, 21431−9.
(22) Yu, H.; Shang, L.; Bian, T.; Shi, R.; Waterhouse, G. I.; Zhao, Y.; Zhou, C.; Wu, L. Z.; Tung, C. H.; Zhang, T. Nitrogen-Doped Porous Carbon Nanosheets Templated from g-C3 N4 as Metal-Free Electrocatalysts for Efficient Oxygen Reduction Reaction. *Adv. Mater.* **2016**, *28*, 5080−6.
(23) Zhang, C. L.; Wang, B. W.; Shen, X. C.; Liu, J. W.; Kong, X. K.; Chuang, S. S. C.; Yang, D.; Dong, A. G.; Peng, Z. M. A nitrogen-doped ordered mesoporous carbon/graphene framework as bifunctional electrocatalyst for oxygen reduction and evolution reactions. *Nano Energy* **2016**, *30*, 503−510.
(24) Graglia, M.; Pampel, J.; Hantke, T.; Fellinger, T. P.; Esposito, D. Nitro Lignin-Derived Nitrogen-Doped Carbon as an Efficient and Sustainable Electrocatalyst for Oxygen Reduction. *ACS Nano* **2016**, *10*, 4364−71.
(25) Dai, L.; Xue, Y.; Qu, L.; Choi, H. J.; Baek, J. B. Metal-free catalysts for oxygen reduction reaction. *Chem. Rev.* **2015**, *115*, 4823−92.
(26) Shao, M.; Chang, Q.; Dodelet, J. P.; Chenitz, R. Recent Advances in Electrocatalysts for Oxygen Reduction Reaction. *Chem. Rev.* **2016**, *116*, 3594−657.
(27) Song, L. T.; Wu, Z. Y.; Zhou, F.; Liang, H. W.; Yu, Z. Y.; Yu, S. H. Sustainable Hydrothermal Carbonization Synthesis of Iron/Nitrogen-Doped Carbon Nanofiber Aerogels as Electrocatalysts for Oxygen Reduction. *Small* **2016**, *12*, 6398−6406.
(28) Wu, Z. Y.; Xu, X. X.; Hu, B. C.; Liang, H. W.; Lin, Y.; Chen, L. F.; Yu, S. H. Iron Carbide Nanoparticles Encapsulated in Mesoporous Fe-N-Doped Carbon Nanofibers for Efficient Electrocatalysis. *Angew. Chem., Int. Ed.* **2015**, *54*, 8179−83.

DOI: 10.1021/acs.chemmater.7b01265
Chem. Mater. 2017, 29, 5617−5628

(29) Lin, L.; Zhu, Q.; Xu, A. W. Noble-metal-free Fe-N/C catalyst for highly efficient oxygen reduction reaction under both alkaline and acidic conditions. *J. Am. Chem. Soc.* **2014**, *136*, 11027−33.
(30) Sasan, K.; Kong, A. G.; Wang, Y.; Chengyu, M.; Zhai, Q. G.; Feng, P. Y. From Hemoglobin to Porous N-S-Fe-Doped Carbon for Efficient Oxygen Electroreduction. *J. Phys. Chem. C* **2015**, *119*, 13545−13550.
(31) Wang, Y.; Kong, A. G.; Chen, X. T.; Lin, Q. P.; Feng, P. Y. Efficient Oxygen Electroreduction: Hierarchical Porous Fe-N-doped Hollow Carbon Nanoshells. *ACS Catal.* **2015**, *5*, 3887−3893.
(32) Niu, W. H.; Li, L. G.; Chen, S. W. Recent Progress in Template-Assisted Synthesis of Nitrogen-Doped Porous Carbons for Oxygen Electroreduction. *J. Electrochem.* **2017**, *23*, 110−122.
(33) Wei, J.; Liang, Y.; Hu, Y.; Kong, B.; Simon, G. P.; Zhang, J.; Jiang, S. P.; Wang, H. A Versatile Iron-Tannin-Framework Ink Coating Strategy to Fabricate Biomass-Derived Iron Carbide/Fe-N-Carbon Catalysts for Efficient Oxygen Reduction. *Angew. Chem., Int. Ed.* **2016**, *55*, 1355−9.
(34) Yang, H. B.; Miao, J.; Hung, S. F.; Chen, J.; Tao, H. B.; Wang, X.; Zhang, L.; Chen, R.; Gao, J.; Chen, H. M.; Dai, L.; Liu, B. Identification of catalytic sites for oxygen reduction and oxygen evolution in N-doped graphene materials: Development of highly efficient metal-free bifunctional electrocatalyst. *Sci. Adv.* **2016**, *2*, e1501122.
(35) Sa, Y. J.; Seo, D. J.; Woo, J.; Lim, J. T.; Cheon, J. Y.; Yang, S. Y.; Lee, J. M.; Kang, D.; Shin, T. J.; Shin, H. S.; Jeong, H. Y.; Kim, C. S.; Kim, M. G.; Kim, T. Y.; Joo, S. H. A General Approach to Preferential Formation of Active Fe-Nx Sites in Fe-N/C Electrocatalysts for Efficient Oxygen Reduction Reaction. *J. Am. Chem. Soc.* **2016**, *138*, 15046−15056.
(36) Guo, D.; Shibuya, R.; Akiba, C.; Saji, S.; Kondo, T.; Nakamura, J. Active sites of nitrogen-doped carbon materials for oxygen reduction reaction clarified using model catalysts. *Science* **2016**, *351*, 361−5.
(37) Lee, J. S.; Park, G. S.; Kim, S. T.; Liu, M.; Cho, J. A highly efficient electrocatalyst for the oxygen reduction reaction: N-doped ketjenblack incorporated into Fe/Fe3C-functionalized melamine foam. *Angew. Chem., Int. Ed.* **2013**, *52*, 1026−30.
(38) Zhu, Y.; Zhang, B.; Liu, X.; Wang, D. W.; Su, D. S. Unravelling the structure of electrocatalytically active Fe-N complexes in carbon for the oxygen reduction reaction. *Angew. Chem., Int. Ed.* **2014**, *53*, 10673−7.
(39) Zitolo, A.; Goellner, V.; Armel, V.; Sougrati, M. T.; Mineva, T.; Stievano, L.; Fonda, E.; Jaouen, F. Identification of catalytic sites for oxygen reduction in iron- and nitrogen-doped graphene materials. *Nat. Mater.* **2015**, *14*, 937−42.
(40) Niu, W.; Li, L.; Liu, X.; Wang, N.; Liu, J.; Zhou, W.; Tang, Z.; Chen, S. Mesoporous N-doped carbons prepared with thermally removable nanoparticle templates: an efficient electrocatalyst for oxygen reduction reaction. *J. Am. Chem. Soc.* **2015**, *137*, 5555−62.
(41) Szakacs, C. E.; Lefevre, M.; Kramm, U. I.; Dodelet, J. P.; Vidal, F. A density functional theory study of catalytic sites for oxygen reduction in Fe/N/C catalysts used in H(2)/O(2) fuel cells. *Phys. Chem. Chem. Phys.* **2014**, *16*, 13654−61.
(42) Chai, G. L.; Hou, Z.; Shu, D. J.; Ikeda, T.; Terakura, K. Active sites and mechanisms for oxygen reduction reaction on nitrogen-doped carbon alloy catalysts: Stone-Wales defect and curvature effect. *J. Am. Chem. Soc.* **2014**, *136*, 13629−40.
(43) Cui, X. Y.; Yang, S. B.; Yan, X. X.; Leng, J. G.; Shuang, S.; Ajayan, P. M.; Zhang, Z. J. Pyridinic-Nitrogen-Dominated Graphene Aerogels with Fe-N-C Coordination for Highly Efficient Oxygen Reduction Reaction. *Adv. Funct. Mater.* **2016**, *26*, 5708−5717.
(44) Zhao, Y.; Kamiya, K.; Hashimoto, K.; Nakanishi, S. Efficient Bifunctional Fe/C/N Electrocatalysts for Oxygen Reduction and Evolution Reaction. *J. Phys. Chem. C* **2015**, *119*, 2583−2588.
(45) Lai, Q.; Su, Q.; Gao, Q.; Liang, Y.; Wang, Y.; Yang, Z.; Zhang, X.; He, J.; Tong, H. In Situ Self-Sacrificed Template Synthesis of Fe-N/G Catalysts for Enhanced Oxygen Reduction. *ACS Appl. Mater. Interfaces* **2015**, *7*, 18170−8.
(46) Liang, H. W.; Liu, J. W.; Qian, H. S.; Yu, S. H. Multiplex templating process in one-dimensional nanoscale: controllable synthesis, macroscopic assemblies, and applications. *Acc. Chem. Res.* **2013**, *46*, 1450−61.
(47) Song, L. T.; Wu, Z. Y.; Liang, H. W.; Zhou, F.; Yu, Z. Y.; Xu, L.; Pan, Z.; Yu, S. H. Macroscopic-scale synthesis of nitrogen-doped carbon nanofiber aerogels by template-directed hydrothermal carbonization of nitrogen-containing carbohydrates. *Nano Energy* **2016**, *19*, 117−127.
(48) Wang, J. L.; Liu, J. W.; Lu, B. Z.; Lu, Y. R.; Ge, J.; Wu, Z. Y.; Wang, Z. H.; Arshad, M. N.; Yu, S. H. Recycling nanowire templates for multiplex templating synthesis: a green and sustainable strategy. *Chem. - Eur. J.* **2015**, *21*, 4935−9.
(49) Wang, K.; Yang, Y.; Liang, H. W.; Liu, J. W.; Yu, S. H. First sub-kilogram-scale synthesis of high quality ultrathin tellurium nanowires. *Mater. Horiz.* **2014**, *1*, 338−343.
(50) Xu, J.; Xin, S.; Liu, J. W.; Wang, J. L.; Lei, Y.; Yu, S. H. Elastic Carbon Nanotube Aerogel Meets Tellurium Nanowires: A Binder- and Collector-Free Electrode for Li-Te Batteries. *Adv. Funct. Mater.* **2016**, *26*, 3580−3588.
(51) Cui, G.; Zhi, L.; Thomas, A.; Kolb, U.; Lieberwirth, I.; Mullen, K. One-dimensional porous carbon/platinum composites for nano-scale electrodes. *Angew. Chem., Int. Ed.* **2007**, *46*, 3464−7.
(52) Qian, H. S.; Yu, S. H.; Gong, J. Y.; Luo, L. B.; Fei, L. F. High-quality luminescent tellurium nanowires of several nanometers in diameter and high aspect ratio synthesized by a poly (vinyl pyrrolidone)-assisted hydrothermal process. *Langmuir* **2006**, *22*, 3830−5.
(53) Giannozzi, P.; Baroni, S.; Bonini, N.; Calandra, M.; Car, R.; Cavazzoni, C.; Ceresoli, D.; Chiarotti, G. L.; Cococcioni, M.; Dabo, I.; Dal Corso, A.; de Gironcoli, S.; Fabris, S.; Fratesi, G.; Gebauer, R.; Gerstmann, U.; Gougoussis, C.; Kokalj, A.; Lazzeri, M.; Martin-Samos, L.; Marzari, N.; Mauri, F.; Mazzarello, R.; Paolini, S.; Pasquarello, A.; Paulatto, L.; Sbraccia, C.; Scandolo, S.; Sclauzero, G.; Seitsonen, A. P.; Smogunov, A.; Umari, P.; Wentzcovitch, R. M. QUANTUM ESPRESSO: a modular and open-source software project for quantum simulations of materials. *J. Phys.: Condens. Matter* **2009**, *21*, 395502.
(54) Garrity, K. F.; Bennett, J. W.; Rabe, K. M.; Vanderbilt, D. Pseudopotentials for high-throughput DFT calculations. *Comput. Mater. Sci.* **2014**, *81*, 446−452.
(55) Marzari, N.; Vanderbilt, D.; De Vita, A.; Payne, M. C. Thermal contraction and disordering of the Al(110) surface. *Phys. Rev. Lett.* **1999**, *82*, 3296−3299.
(56) Baroni, S.; de Gironcoli, S.; Dal Corso, A.; Giannozzi, P. Phonons and related crystal properties from density-functional perturbation theory. *Rev. Mod. Phys.* **2001**, *73*, 515−562.
(57) Ping, Y.; Nielsen, R. J.; Goddard, W. A., 3rd The Reaction Mechanism with Free Energy Barriers at Constant Potentials for the Oxygen Evolution Reaction at the IrO(2) (110) Surface. *J. Am. Chem. Soc.* **2017**, *139*, 149−155.
(58) Sundararaman, R.; Goddard, W. A., 3rd The charge-asymmetric nonlocally determined local-electric (CANDLE) solvation model. *J. Chem. Phys.* **2015**, *142*, 064107.
(59) Petrosyan, S. A.; Briere, J. F.; Roundy, D.; Arias, T. A. Joint density-functional theory for electronic structure of solvated systems. *Phys. Rev. B: Condens. Matter Mater. Phys.* **2007**, *75*, 205105.
(60) Ping, Y.; Sundararaman, R.; Goddard, W. A., III Solvation effects on the band edge positions of photocatalysts from first principles. *Phys. Chem. Chem. Phys.* **2015**, *17*, 30499−509.
(61) Semenov, A. V.; Pergament, A. L.; Pikalev, A. A. Raman spectroscopy of melamine-formaldehyde resin microparticles exposed to processing in complex plasma. *J. Raman Spectrosc.* **2016**, *47*, 1293−1297.
(62) Chen, L. M.; Hu, P. G.; Deming, C. P.; Wang, N.; Lu, J. E.; Chen, S. W. Intervalence Charge Transfer of Ruthenium-Nitrogen Moieties Embedded within Nitrogen-Doped Graphene Quantum Dots. *J. Phys. Chem. C* **2016**, *120*, 13303−13309.
(63) Ong, W.-J.; Tan, L.-L.; Chai, S.-P.; Yong, S.-T. Heterojunction engineering of graphitic carbon nitride (gC 3 N 4) via Pt loading with

DOI: 10.1021/acs.chemmater.7b01265
Chem. Mater. 2017, 29, 5617−5628

improved daylight-induced photocatalytic reduction of carbon dioxide to methane. *Dalton Trans.* **2015**, *44*, 1249−1257.
(64) Xing, Z.; Ju, Z. C.; Zhao, Y. L.; Wan, J. L.; Zhu, Y. B.; Qiang, Y. H.; Qian, Y. T. One-pot hydrothermal synthesis of Nitrogen-doped graphene as high-performance anode materials for lithium ion batteries. *Sci. Rep.* **2016**, *6*, 26146.
(65) Niu, W.; Li, L.; Liu, J.; Wang, N.; Li, W.; Tang, Z.; Zhou, W.; Chen, S. Graphene-Supported Mesoporous Carbons Prepared with Thermally Removable Templates as Efficient Catalysts for Oxygen Electroreduction. *Small* **2016**, *12*, 1900−8.
(66) Liu, X. J.; Zou, S. Z.; Chen, S. W. Ordered mesoporous carbons codoped with nitrogen and iron as effective catalysts for oxygen reduction reaction. *Nanoscale* **2016**, *8*, 19249−19255.
(67) Jiang, W. J.; Gu, L.; Li, L.; Zhang, Y.; Zhang, X.; Zhang, L. J.; Wang, J. Q.; Hu, J. S.; Wei, Z.; Wan, L. J. Understanding the High Activity of Fe-N-C Electrocatalysts in Oxygen Reduction: Fe/Fe3C Nanoparticles Boost the Activity of Fe-N(x). *J. Am. Chem. Soc.* **2016**, *138*, 3570−8.
(68) Yang, S.; Feng, X.; Wang, X.; Mullen, K. Graphene-based carbon nitride nanosheets as efficient metal-free electrocatalysts for oxygen reduction reactions. *Angew. Chem., Int. Ed.* **2011**, *50*, 5339−43.
(69) Artyushkova, K.; Serov, A.; Rojas-Carbonell, S.; Atanassov, P. Chemistry of Multitudinous Active Sites for Oxygen Reduction Reaction in Transition Metal-Nitrogen-Carbon Electrocatalysts. *J. Phys. Chem. C* **2015**, *119*, 25917−25928.
(70) Zhou, D.; Yang, L. P.; Yu, L. H.; Kong, J. H.; Yao, X. Y.; Liu, W. S.; Xu, Z. C.; Lu, X. H. Fe/N/C hollow nanospheres by Fe(III)-dopamine complexation-assisted one-pot doping as nonprecious-metal electrocatalysts for oxygen reduction. *Nanoscale* **2015**, *7*, 1501−1509.
(71) Meng, F. L.; Wang, Z. L.; Zhong, H. X.; Wang, J.; Yan, J. M.; Zhang, X. B. Reactive Multifunctional Template-Induced Preparation of Fe-N-Doped Mesoporous Carbon Microspheres Towards Highly Efficient Electrocatalysts for Oxygen Reduction. *Adv. Mater.* **2016**, *28*, 7948−7955.
(72) Pei, G. X.; Liu, X. Y.; Wang, A.; Lee, A. F.; Isaacs, M. A.; Li, L.; Pan, X.; Yang, X.; Wang, X.; Tai, Z.; Wilson, K.; Zhang, T. Ag Alloyed Pd Single-Atom Catalysts for Efficient Selective Hydrogenation of Acetylene to Ethylene in Excess Ethylene. *ACS Catal.* **2015**, *5*, 3717−3725.
(73) Sa, Y. J.; Park, C.; Jeong, H. Y.; Park, S. H.; Lee, Z.; Kim, K. T.; Park, G. G.; Joo, S. H. Carbon nanotubes/heteroatom-doped carbon core-sheath nanostructures as highly active, metal-free oxygen reduction electrocatalysts for alkaline fuel cells. *Angew. Chem., Int. Ed.* **2014**, *53*, 4102−6.
(74) Zhang, P.; Sun, F.; Xiang, Z. H.; Shen, Z. G.; Yun, J.; Cao, D. P. ZIF-derived in situ nitrogen-doped porous carbons as efficient metal-free electrocatalysts for oxygen reduction reaction. *Energy Environ. Sci.* **2014**, *7*, 442−450.
(75) Zhou, Z. Y.; Kang, X.; Song, Y.; Chen, S. Enhancement of the electrocatalytic activity of Pt nanoparticles in oxygen reduction by chlorophenyl functionalization. *Chem. Commun.* **2012**, *48*, 3391−3.
(76) Xing, T.; Zheng, Y.; Li, L. H.; Cowie, B. C.; Gunzelmann, D.; Qiao, S. Z.; Huang, S.; Chen, Y. Observation of active sites for oxygen reduction reaction on nitrogen-doped multilayer graphene. *ACS Nano* **2014**, *8*, 6856−62.
(77) Kattel, S.; Atanassov, P.; Kiefer, B. A density functional theory study of oxygen reduction reaction on non-PGM Fe-Nx-C electrocatalysts. *Phys. Chem. Chem. Phys.* **2014**, *16*, 13800−6.
(78) Zhang, J.; Wang, Z.; Zhu, Z. P.; Wang, Q. A Density Functional Theory Study on Mechanism of Electrochemical Oxygen Reduction on FeN4-Graphene. *J. Electrochem. Soc.* **2015**, *162*, F796−F801.
(79) Kattel, S.; Wang, G. A density functional theory study of oxygen reduction reaction on Me−N4 (Me = Fe, Co, or Ni) clusters between graphitic pores. *J. Mater. Chem. A* **2013**, *1*, 10790.
(80) Viswanathan, V.; Hansen, H. A.; Rossmeisl, J.; Norskov, J. K. Universality in Oxygen Reduction Electrocatalysis on Metal Surfaces. *ACS Catal.* **2012**, *2*, 1654−1660.
(81) Li, M. T.; Zhang, L. P.; Xu, Q.; Niu, J. B.; Xia, Z. H. N-doped graphene as catalysts for oxygen reduction and oxygen evolution reactions: Theoretical considerations. *J. Catal.* **2014**, *314*, 66−72.
(82) McClure, J. P.; Borodin, O.; Olguin, M.; Chu, D.; Fedkiw, P. S. Sensitivity of Density Functional Theory Methodology for Oxygen Reduction Reaction Predictions on Fe-N-4-Containing Graphitic Clusters. *J. Phys. Chem. C* **2016**, *120*, 28545−28562.
(83) Yu, L.; Pan, X. L.; Cao, X. M.; Hu, P.; Bao, X. H. Oxygen reduction reaction mechanism on nitrogen-doped graphene: A density functional theory study. *J. Catal.* **2011**, *282*, 183−190.
(84) Towns, J.; Cockerill, T.; Dahan, M.; Foster, I.; Gaither, K.; Grimshaw, A.; Hazlewood, V.; Lathrop, S.; Lifka, D.; Peterson, G. D. XSEDE: Accelerating Scientific Discovery. *Comput. Sci. Eng.* **2014**, *16*, 62−74.

DOI: 10.1021/acs.chemmater.7b01265
Chem. Mater. 2017, 29, 5617−5628